Improving the Electric Sector of a Cycloidal Mass Analyzer

by

Eung Hyun (William) Kim

Department of Electrical and Computer Engineering
Duke University

Date:_____

Approved:

_____
Jeffrey T. Glass, Supervisor

_____
Michael E. Gehm

_____
William T. Joines

Thesis submitted in partial fulfillment of
the requirements for the degree of Master of Science in the Department of
Electrical and Computer Engineering in the Graduate School
of Duke University

2017

ABSTRACT

Improving the Electric Sector of a Cycloidal Mass Analyzer

by

Eung Hyun (William) Kim

Department of Electrical and Computer Engineering
Duke University

Date:_____

Approved:

_____
Jeffrey T. Glass, Supervisor

_____
Michael E. Gehm

_____
William T. Joines

An abstract of a thesis submitted in partial
fulfillment of the requirements for the degree
of Master of Science in the Department of
Electrical and Computer Engineering in the Graduate School of
Duke University

2017

Abstract

Aperture coding has been utilized in mass spectrometry to enable miniaturization of the instrument while maintaining resolution and throughput. Successful implementation of aperture coding in a cycloidal mass analyzer requires uniform magnetic and electric fields in the sector region. This work shows through finite element simulation that the compatibility between a cycloidal mass analyzer and aperture coding has been improved by the development of a novel electric sector with a highly uniform electric field. COMSOL 5.2a was utilized as the primary finite element analysis tool, and MATLAB R2016b was used to generate most figures.

Contents

List of Figures

List of Tables

Acknowledgements

The information, data, or work presented herein was funded in part by the Advanced Research Projects Agency-Energy (ARPA-E), U.S. Department of Energy, under Award Number DE-AR0000546. The views and opinions of authors expressed herein do not necessarily state or reflect those of the United States Government or any agency thereof.

1. Introduction

Detecting benzene, toluene, ethylbenzene, and xylene (BTEX) as well as methane and other natural gas components in real time is crucial in oil refinery settings [1-2]. Currently, a general method for BTEX detection involves using sorbent tubes for lab analysis or photoionization detectors in the field that are limited in specificity. The EPA regulations on measuring volatile organic compounds list the process taking approximately 2 weeks [3]. Due to many harmful effects of volatile organic compounds [2], this timeline is not ideal especially for situations in which a leak may be present. Thus, a real-time measurement to immediately identify a leak is necessary.

As part of the DOE ARPA-E MONITOR program, we are developing a portable, real-time coded aperture miniature mass spectrometer for environmental sensing. Our instrument will be able to detect the aforementioned volatile organic compounds as well as other constituents of natural gas. Moreover, an advantage of this instrument will be its size and portability. There are several challenges to achieving this goal, perhaps the most significant of which is the miniaturization aspect. This work demonstrates a partial solution to this challenge by increasing the compatibility of aperture coding with a cycloidal mass analyzer.

Aperture Coding is a technique recently demonstrated in sector mass spectrometry to increase throughput without sacrificing resolution [4-7]. In a conventional sector mass analyzer, a slit at the exit of the ion source is used to define

resolution. Aperture coding replaces a single slit with a patterned array of slits. The resulting pattern at the detector can then be computationally reconstructed to determine the components of an analyte. The use of multiple slits allows for greatly increased throughput without sacrificing resolution. An advantage of this property is that it enables reducing the instrument size while maintaining resolution and throughput.

Aperture Coding has been demonstrated in several types of sector mass analyzers. Aperture coding was first utilized in a simple 90-degree magnetic sector. Replacing a conventional single slit with a 1-dimensional (1D) or 2-dimenstional (2D) coded apertures enabled a throughput increase by over an order of magnitude without loss of resolution [4-5]. However, the instrument had limited mass range and resolution because it did not correct for the ion initial energy and angular distributions. Russell et al. demonstrated another application of aperture coding using Mattauch-Herzog geometry. The Mattauch-Herzog Mass Spectrometer (MS) is a mass analyzer employing an electric and magnetic sector that corrects for energy and angular dispersion from the ion source to first order. Russell et al. showed that this instrument is compatible with aperture coding via simulation and experiment [6]. However, the resulting imaging quality was relatively poor due to fringing fields and the electric sector width limiting the aperture coding complexity.

Cycloidal mass analyzers employ perpendicularly oriented magnetic and electric fields. Charged particles travelling in a perpendicular – relative to the particle's velocity

– magnetic field exhibit a circular trajectory. Particles travelling in a parallel electric field will exhibit translation. Together, these perpendicularly orientated fields cause the particle to travel in a cycloidal trajectory [8].

Equation 1.1 below describes the motion of an ion in perpendicularly oriented uniform electric and magnetic fields.

$$a_i = \frac{m_i}{z}\frac{2\pi E}{B^2} \tag{1.1}$$

a_i is the distance from the ion source exit slit to the point of contact with the detector, m_i is the mass of the i^{th} ion, z is the charge on the ion, E is the applied uniform electric field, and B is the applied uniform magnetic field. Note that the distance a_i does not depend on the particles' initial energy and direction. Therefore, a cycloidal mass analyzer is double focusing to all orders, and thus is ideal for application of aperture coding.

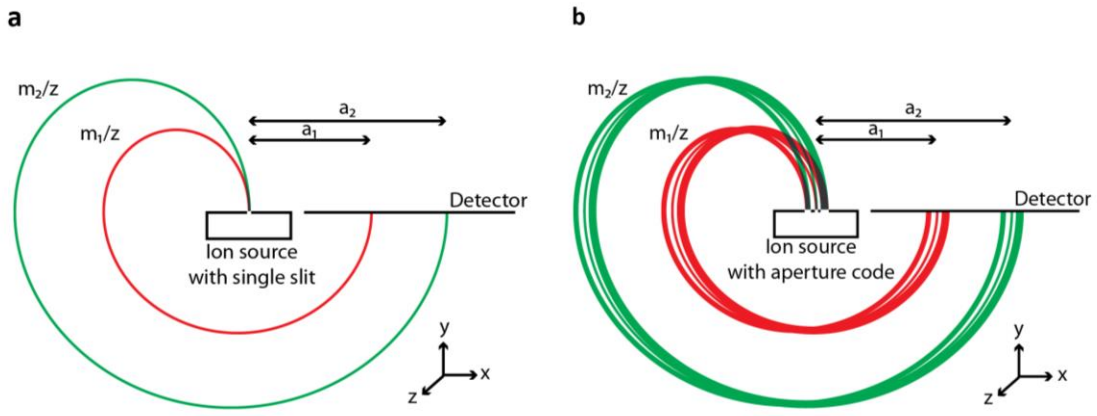

Figure 1: Cycloidal ion trajectories for (a) conventional single slit instrument (b) coded aperture instrument for two different mass to charge ratios m_1/z and m_2/z. Green paths represent the trajectories of particles of mass m_2, while red paths represent trajectories of particles of mass m_1.

Figure 1**a** above shows the cycloidal ion trajectories for two different mass to charge ratios in a conventional single slit instrument, while Figure 1**b** shows the trajectories for a coded aperture instrument. Note that in Figure 1**b**, perfect images of the aperture coding at the ion source are projected onto the detector – thus demonstrating that cycloidal mass analyzers are inherently compatible with aperture coding.

To fully realize the cycloidal mass analyzer double focusing properties, the magnetic and electric fields must be uniform. Robinson et al. studied the effects of non-uniform fields in cycloidal mass analyzers. They concluded that for the electric field, a non-uniformity will shift the focal point away from the detector plane, or the resolving slit [9]. By extension, a non-uniform electric field will yield a poor imaging of the coded aperture at the detector. Therefore, achieving a sufficiently uniform electric and

magnetic fields is critical for successful application of coded apertures to cycloidal mass analyzers.

This thesis investigates the imaging performance of various electric sector configurations for a cycloidal mass analyzer using the magnetic sector described in Landry et al. [10]. Finite element simulations and ion trajectory calculations are utilized for this research. The first electric sector configuration, Configuration 1, which is analyzed in 3-dimensional space, is similar to those previously reported in the literature [11] and used in the miniature prototype discussed in Amsden et al. [7]. Then, several other configurations are analyzed in 2-dimensional space to examine how to improve the electric field profile of the sector. The results of the 2 dimensional simulations suggest a new electric sector configuration, Configuration 2, which was simulated also in 3-dimensional space. Configuration 2 yields significantly improved aperture imaging quality compared to that of Configuration 1.

2. Methods

This section outlines in detail how each simulation space was set up. The first subsection describes the simulations done in 2-dimensional space, while the second subsection describes the simulations done in 3-dimensional space.

2.1 2D Simulations

2.1.1 Geometry

The electric sector geometries of 2-dimensional configurations were first generated in AutoCAD 2016.

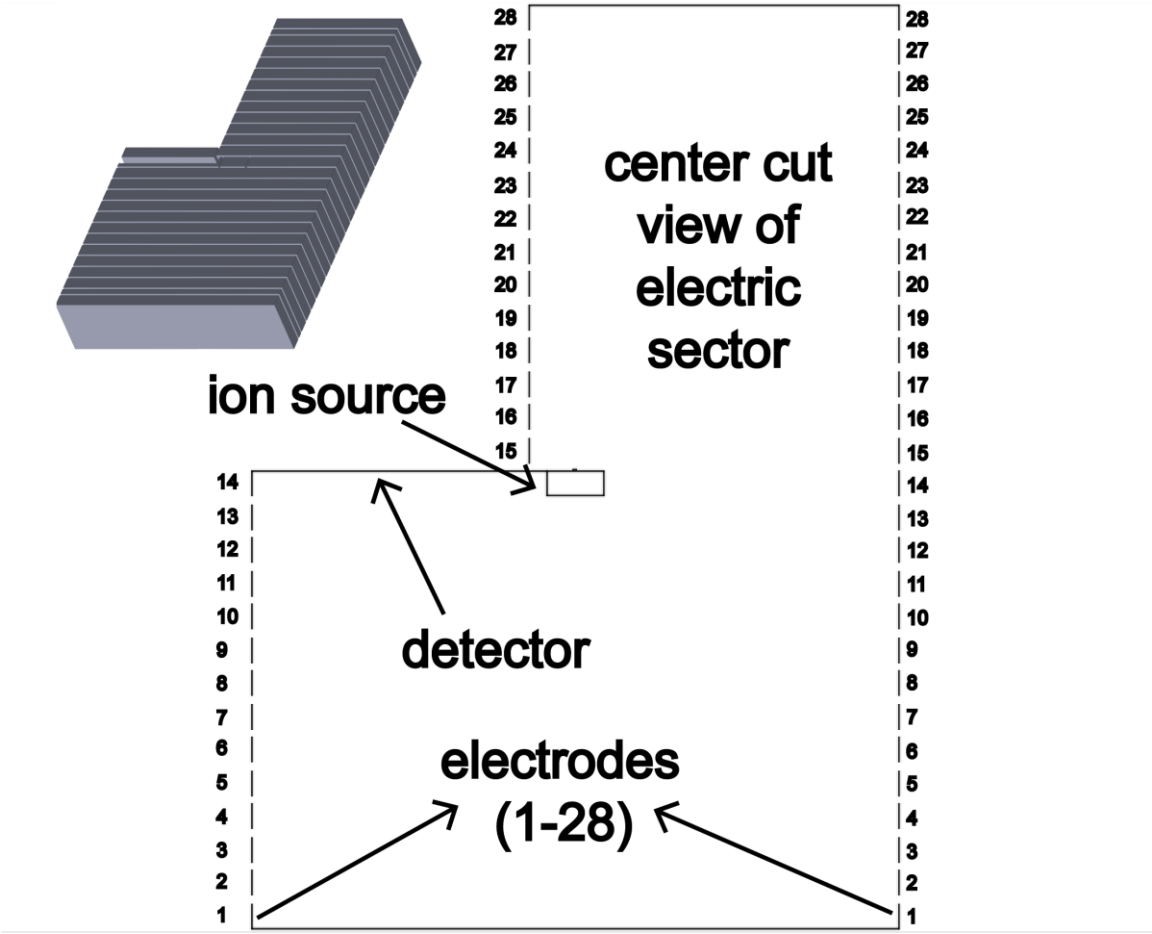

Figure 2: 2D AutoCAD model of a plane cut through the center of the electric sector (see inset) which is placed between the magnets (see Figure 4). Each pair of segments of the dashed black lines labeled 1 to 28 represents a cut view of an electrode that ban be biased independently from the adjacent electrodes.

Figure 2 shows an example electric sector configuration in AutoCAD. It is an L-shaped box of dimensions 94.5 mm x 78 mm. The sector is composed of parallel dashed lines, spaced 0.5 mm apart. Each set of parallel lines (one to the left of the sector and one

to the right of the sector) represent one electrode. Thus, overall, these dashed lines essentially represent 28 electrodes.

Several iterations of the above configuration were created with slight variations. After examining the electric field profiles of each of them, some were discarded because they did not provide any useful information while others were analyzed and provided a basis for future simulations. More details are outlined in the 2D Simulations subsection in the Results section.

2.1.2 Materials

The electrodes, ion source, and the detector were labeled as copper.

Table 1: Copper Properties

Property	Value	Unit
Relative Permeability	1	-
Relative permittivity	1	-
Electrical Conductivity	5.998E7	S/m
Heat capacity at constant pressure	385	J/(kg·K)
Surface emissivity	0.5	-
Density	870	kg/m^3
Thermal conductivity	400	W/(m·K)
Reference resistivity	1.72E-8	Ω·m
Resistivity temperature coefficient	3.9E-3	1/K
Reference temperature	273.15	K

Table 1 above shows the specific parameters associated with copper in this simulation space. Note that the choice of conductor was arbitrary. This is because the main objective is to bias the electrodes at the desired potentials, but the means to achieve this goal is not significant.

Table 2: Air Properties

Property	Value	Unit
Relative permeability	1	-
Relative permittivity	1	-
Dynamic viscosity	eta(T[1/K])	Pa·s
Ratio of specific heats	1.4	-
Electrical conductivity	0	S/m
Heat capacity at constant pressure	Cp(T[1/K])[J/(kg·K)]	J/(kg·K)
Density	Rho(pA[1/Pa], T[1/K])	kg/m^3
Thermal conductivity	K(T[1/K])	W/(m·K)
Speed of sound	cs(T[1/K])	m/s
Refractive index, real part	1	-
Refractive index, imaginary part	0	-

The rest of the simulation space in Figure 2, which is essentially all region between and around the white lines, was labeled as air. The specific parameters can be seen in Table 2 above.

2.1.3 Magnetics

In 2-dimensional simulations, an ideal magnetic field of 0.3 T coming out of the page from the point of view of Figure 2 was applied to the sector. The reason for this is that the purpose of the 2D simulations is to examine the electric field profile of the sector. Moreover, these simulations are primarily to estimate the effects in 3-dimensional space. Under ideal field conditions, cycloidal mass analyzers do not exhibit dispersion in the z-axis (Figure 1). While non-ideal conditions affect the trajectory such that dispersion in the z-axis does exist, we determined that this dispersion is small enough that simplifying the simulations to a cross sectional plane in the middle of the sector (2D simulation) would yield useful information as well. Thus, an ideal magnetic field was applied to simplify the overall process.

.

2.1.4 Electrostatics

The electrodes were biased according to Equation 1.2 below.

$$V_i = \left(\frac{i-14}{28} \right) Ed \tag{1.2}$$

V_i represents the potential on the electrodes, i represents the electrode number from 0 to 28 starting from the bottom electrode to the top electrode, E represents the desired electric field, and d represents the height of the sector.

Equation 1.2 above was derived from the fact that electric field is the negative gradient of potential. Solving for the differential equation, the following equation is obtained.

$$V = -Ey \tag{1.3}$$

V represents the potential, E represents the desired electric field in the y-coordinate. The $\left(\frac{i-14}{28}\right)d$ term in Equation 1.2 represents the y-coordinate.

Note that the detector is grounded. However, to optimize the field uniformity, the potential on the ion source changes depending on the specific configuration. These details are outlined more specifically in the Results section.

2.1.5 Mesh

The maximum element size and the minimum element size were set to 1.1 mm and 0.00022 mm respectively. Since the minimum mesh size, 0.00022 mm, is roughly 5 orders of magnitude smaller than the sector dimensions, we decided that this number was well suited to produce a mesh that would allow us to examine the electric field profile in great detail. Note a visual representation of the meshed element is not provided since the mesh size is too small. The entire meshed graph appears as one

rectangle of uniform color, and thus a figure would not provide any meaningful information.

2.1.6 Fields Study

After setting up the geometry, materials, magnetics, electrostatics, and mesh, COMSOL 5.2a's Fields Study module was utilized to solve for the electric field magnitude in the sector region.

2.1.7 Data Generation and Analysis

As aforementioned, the simulations were run in COMSOL 5.2a. The resulting electric field magnitude profile was graphed and the data was exported to MATLAB 2016b for further analysis.

2.2 3D Simulations

The primary goal of this research is to increase the compatibility between cycloidal mass analyzers and aperture coding. Since the sector's field profile as well as particle trajectory with aperture coding cannot be analyzed in 2D, these 3D simulations were necessary to ensure that the goal of this research is achieved.

2.2.1 Geometry

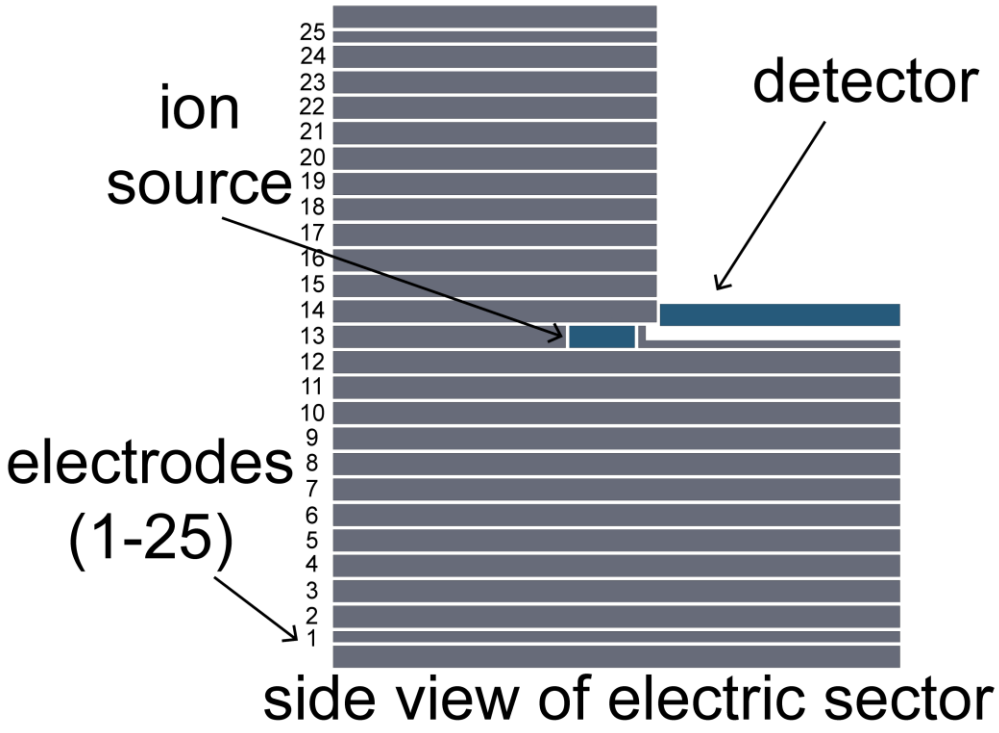

Figure 3: Example side view of electric sector configuration utilized for 3D simulations. Locations of the ion source and detector are labeled in the figure. The sector is composed of 25 electrodes spaced 0.5 mm apart. The numbers in the figure represent electrode number, starting from 1 at the bottom electrode to 25 at the top electrode.

The components of the overall system were generated using SOLIDWORKS 2016. The reason for switching from AutoCAD in 2D to SOLIDWORKS in 3D was that we felt SOLIDWORKS was much better for designing in 3-dimensional space. First, the electric sector was completed as seen in Figure 3 above. It is an L-shaped box of dimensions 91 x 78 x 14 mm. The electric sector is composed of 25 parallel rectangular electrodes, spaced 0.5 mm apart with caps on the top and bottom electrically connected

to the end electrodes. 23 of the electrodes are 3 mm wide while the electrodes adjacent to the top and bottom caps are 1.5 mm wide. The center electrode with the ion source and detector starts at 3 mm wide, but reduces to 1 mm in the region containing the detector to allow positioning of the detector plane at the midpoint of the center electrode. Note that the ion source, of dimension 3 x 9 x 14 mm, is level with the neighboring electrodes, similar to the configuration discussed by Blasé et al. [11]. This ion source location is relevant for only Configuration 1. The location will change from Configuration 1 to Configuration 2. This detail is discussed in more depth in the Results section. Note that there is an airbox that is comparable to the electric sector dimension placed within the sector (not shown in Figure 3). This box helps to control the mesh size within the sector during simulations.

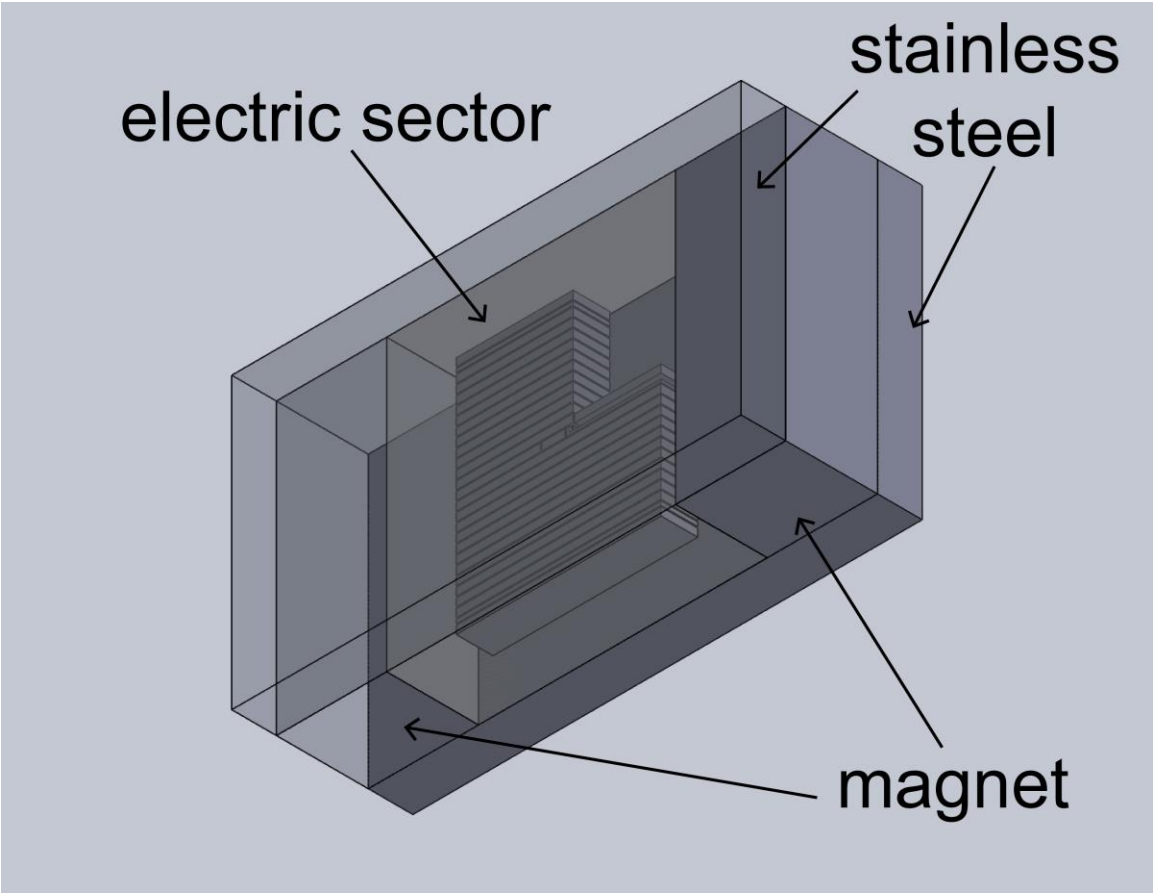

Figure 4: Electric Sector within the magnet region. There are two stainless steel plates, located to the front and back of the sector as seen in the figure. The two magnet bars are located to the left and right of the sector as seen in the figure.

Next, the sector was placed within a magnet geometry as seen in Figure 4 above. The magnets are of dimensions 42 x 110 x 35 mm, while the stainless-steel components are of dimensions 194 x 110 x 17 mm. The justification for this geometry is described by Landry et. al [10].

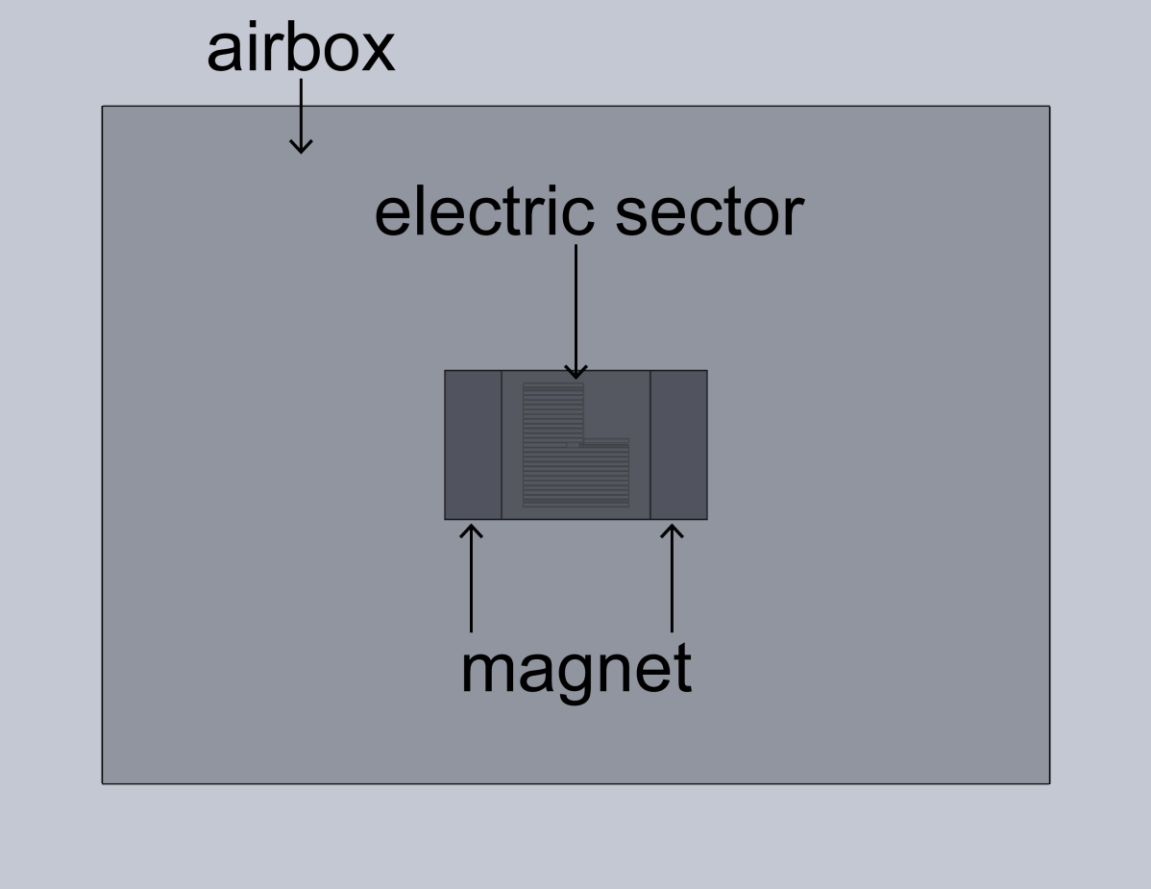

Figure 5: Example of a complete 3D configuration space. Note the large airbox placed around the electric sector and magnet region.

Finally, a large box was designed to encompass the entirety of the system. The dimensions of the box are 700 x 500 x 600 mm. This box was placed to eliminate any potential edge effects of the electric and magnetic field in simulation. More specifically, this box provides a large volume such that the field lines from the sector region are not bound by artificial boundaries at the edge of the sector. The overall system can be seen

in Figure 5 above. Note that there is an airbox of dimensions 152 x 110 x 35 mm surrounding the electric sector, which helps set the mesh size of the region surrounding the electric sector.

After designing the sector in SOLIDWORKS, the files were exported to COMSOL 5.2a as STL files.

.

2.2.2 Materials

The relevant property for the magnet components is the remanent flux density, which was set to $0\mathbf{x} + 0\mathbf{y} + 1.4\mathbf{z}$ T.

Table 3: Copper Properties

Property	Value	Unit
Relative Permeability	1	-
Relative permittivity	1	-
Electrical Conductivity	5.998E7	S/m
Heat capacity at constant pressure	385	J/(kg·K)
Surface emissivity	0.5	-
Density	870	kg/m^3
Thermal conductivity	400	W/(m·K)
Reference resistivity	1.72E-8	Ω·m
Resistivity temperature coefficient	3.9E-3	1/K
Reference temperature	273.15	K

The properties of the electric sector components were set as seen in Table 3 above. These are the default parameters for copper in COMSOL 5.2a. Once again, the exact type of

conductor was arbitrary, as the primary concern was the voltage on the electrodes rather than the means of applying those voltages.

Table 4: Air Properties

Property	Value	Unit
Relative permeability	1	-
Relative permittivity	1	-
Dynamic viscosity	eta(T[1/K])	Pa·s
Ratio of specific heats	1.4	-
Electrical conductivity	0	S/m
Heat capacity at constant pressure	Cp(T[1/K])[J/(kg·K)]	J/(kg·K)
Density	Rho(pA[1/Pa], T[1/K])	kg/m^3
Thermal conductivity	K(T[1/K])	W/(m·K)
Speed of sound	cs(T[1/K])	m/s
Refractive index, real part	1	-
Refractive index, imaginary part	0	-

The rest of the system, which includes the box inside the electric sector, the box surrounding the electric sector, and the large box surrounding the entire system were labeled as air. These boxes were placed such that the mesh size within and around the sector could be controlled and thus produce a finely meshed region. The airbox properties can be seen in Table 4 above.

2.2.3 Magnetics

The remanent flux density value discussed in the previous subsection yielded a magnetic field profile of approximately 0.3 T in the negative z-axis (into the page, from the point of view of Figure 2) within the electric sector region. This value was taken from simulation results.

.

2.2.4 Electrostatics

The electric sector electrodes were biased according to Equation 1.4,

$$V_i = \left(\frac{i-13}{25} \right) Ed \tag{1.4}$$

where V_i represents the electrode voltage, i represents the specific electrode numbered from 0 to 25 starting from the bottom electrode to the top electrode, d represents the distance between the top cap and bottom cap, and E represents the desired electric field.

Equation 1.4 above was derived from the same principle explained using Equation 1.3. The $\left(\frac{i-13}{25}\right)d$ term represents the y-coordinate.

2.2.5 Mesh

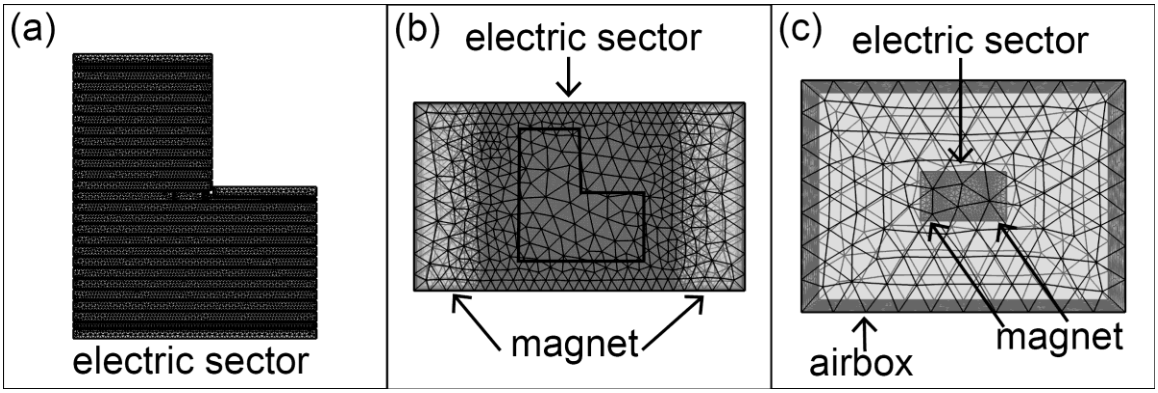

Figure 6: Illustrations of the mesh utilized in computing the electric and magnetic field to determine ion trajectories. (a) meshed electric sector component (b) meshed electric sector and magnet component (c) meshed entire 3D simulation space.

Figure 6 above shows the mesh created and utilized for all 3-dimensional simulations. The sector mesh was created with a maximum elements size of 1.6 mm and minimum element size of 0.005 mm. The resulting meshed element can be seen in Figure 6**a**. The surrounding magnet region mesh was created with 1.4 mm and 0.14 mm

element sizes respectively. The resulting mesh element can be seen in Figure 6**b**. Finally, the domain airbox mesh was created with 70 mm and 12.6 mm element sizes respectively. The resulting mesh element can be seen in Figure 6**c**. Since the sector region is the most significant for analyzing field profiles and particle trajectories, it was created with the smallest mesh size. The mesh sizes of other regions were set such that the simulation would complete in a reasonable amount of time.

2.2.6 Fields Study

COMSOL's Fields Study module was utilized to obtain the electric and magnetic field profile. The details regarding the electric field are outlined in the Results section. The magnetic field in the sector region is approximately 0.3 T, as desired, and the details are discussed more in depth by Landry et. al [10].

2.2.7 Particle Tracing

For the final step, COMSOL's Particle Trajectory Study Module was utilized to obtain the particle trajectory information. This step was done to analyze the aperture imaging quality at the detector. The initial ion conditions included an energy of 14±2 eV and angular spread of 0±9.5 degrees. Note that these initial values were obtained from experiments conducted by Herr et al. [12]. The particle tracing step size was set to 1E-7 s.

This time step was determined by first calculating the approximate time of flight of a 20 amu particle from the ion source to the detector – 5E-5 s. Then, this number was divided by 500 to create time steps of 1E-7 s. The number 500 was chosen to achieve the best balance between obtaining a smooth particle trajectory and the simulation completing in a reasonable amount of time.

2.2.8 Data Generation and Analysis

After running the particle trajectory simulation, the particle count and coordinate data were taken at the detector plane to determine the location and intensity of particles hitting the detector (Poincaré data). This information was exported and histograms were created and formatted in MATLAB version R2016b. The resolving power data calculated at the end of each Results subsection were generated in MATLAB as well.

3. Results

This chapter first discusses results of 3D simulations of an initial configuration ("Configuration 1") of the system that has been utilized experimentally in a coded aperture miniature mass spectrometer prototype as described in a separate paper [7]. Although this electric sector enabled aperture code imaging, improvements in imaging quality would enhance performance. After examining the electric field profile of Configuration 1, we determined that improving the field around the ion source region would likely improve the imaging quality. Configurations expected to improve performance were then simulated in 2D to determine which was the most promising. 2D simulations were utilized in this step to enable rapid assessment of the performance. Finally, the most promising of the configurations (referred to as "Configuration 2") was simulated in 3D to obtain complete quantitative information about performance.

3.1 Configuration 1

The electric sector is an L-shaped box of dimensions 91 x 78 x 14 mm. Figure 7**a** shows a CAD model of the first electric sector configuration. It is composed of 25 parallel rectangular electrodes, spaced 0.5 mm apart with caps on the top and bottom electrically connected to the end electrodes. 23 of the electrodes are 3 mm wide while the electrodes near the top and bottom caps are 1.5 mm wide. The center electrode with the ion source and detector starts at 3 mm wide, but reduces to 1 mm in the region

containing the detector to allow positioning of the detector plane at the midpoint of the center electrode. Note that the ion source, of dimension 3 x 9 x 14 mm, is level with the neighboring electrodes, similar to the configuration discussed by Blasé et al. [11] .

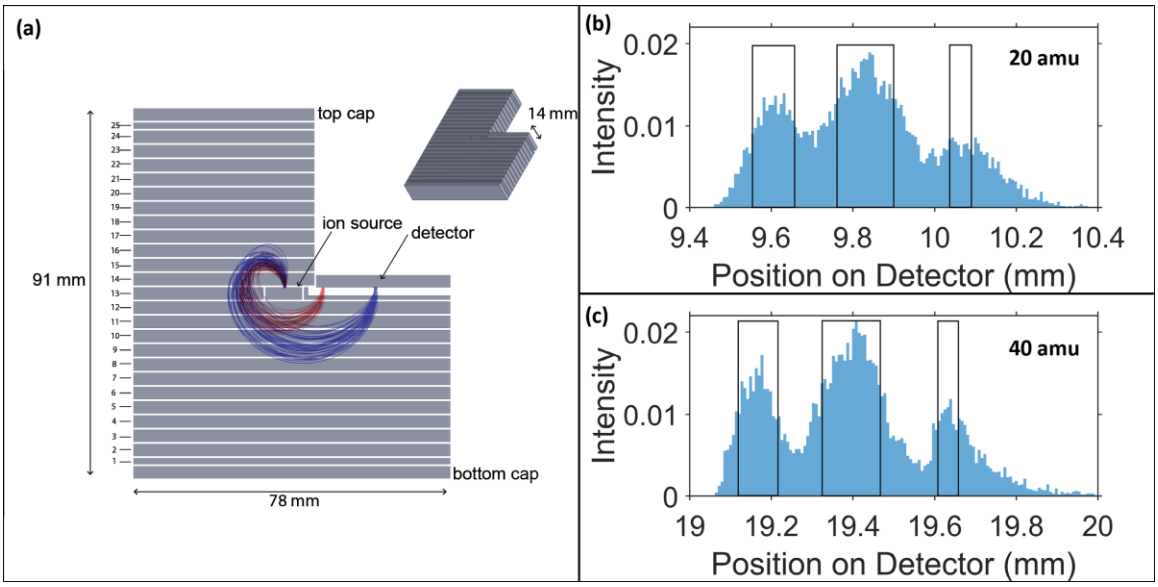

Figure 7: (a) Configuration 1 Electric Sector. Red lines represent 20 amu ion trajectories while blue lines represent 40 amu ion trajectories. Electrodes are numbered 1 to 25 starting from the electrode closest to the bottom cap. (b) Configuration 1 Imaging Quality at Detector for 20 amu (c) Configuration 1 Imaging Quality at Detector for 40 amu

The electrodes are biased according to Equation 1.4 described in Methods section. In this arrangement, the center electrode (electrode #13), which aligns with the ion source and detector is at ground. Furthermore, the ion source and detector are also held at ground.

Using particle tracing of ions with mass to charge ratios of 20 and 40 amu, this electric sector configuration yields aperture images at the detector as seen in Figure 7**b** and Figure 7**c**. Figure 7**b** is the detector image for ions of mass to charge ratio 20 amu while Figure 7**c** shows the detector image for ions of 40 amu. The black rectangles in both figures represent the S-11 aperture pattern used at the exit of the ion source. Under ideal conditions, the detector image would perfectly match these rectangles. Here, the aperture image is blurred slightly (i.e., ions are detected outside of the ideal rectangles shown in the figure) and the aperture image for mass to charge 40 amu appears slightly less blurred than the aperture image at 20 amu.

Figure 8**a** shows a color map of the normalized electric field in a slice through the center of the electric sector. Overall, the field is uniform in most regions except near the at the top and bottom caps of the sector and around the ion source. As the ion trajectories will not pass close to the top and bottom caps, it is unlikely that the field uniformity here affects the aperture imaging. However, as mentioned above, the entire ion source is biased at 0 V. Thus, the field around this region varies significantly.

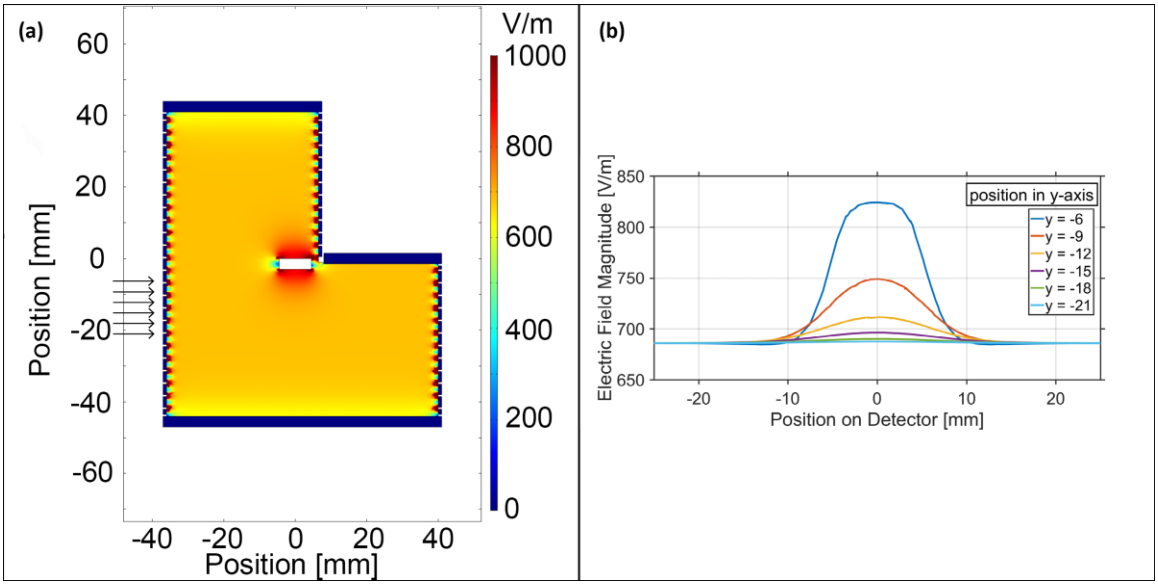

Figure 8: (a) Configuration 1 Electric Field Magnitude Profile (b) Configuration 1 Electric Field Magnitude Near Ion Source Region

Figure 8**b** shows a plot of the electric field along lines indicated by arrows in Figure 8**a**, the electric field magnitude around the ion source region. Equation 1.1 indicates that particles of lower mass will hit the detector at a smaller a_i, which is to say that particles of lower mass will exhibit a cycloidal trajectory of smaller radius. Since the trajectory of 20 amu ions is closer to the ion source, the particles are subject to more electric field non-uniformity. Thus, due to the poor field uniformity, imaging for lower mass ions is worse than that of higher mass ions, as seen in Figure 8**b** and Figure 8**c**.

In order to calculate the resolving power of this sector configuration, another set of simulations was conducted with a regular slit – 0.05 x 1 mm - instead of an aperture

code. Because aperture coding peaks could overlap at the detector, establishing resolving power using aperture coding can be quite difficult. Therefore, a slit was utilized to simplify the process. The Poincaré data at the detector plane was exported to calculate the resolving power defined by the International Union of Pure and Applied Chemistry [13], which is the width of two points that is 5 % of the maximum peak height.

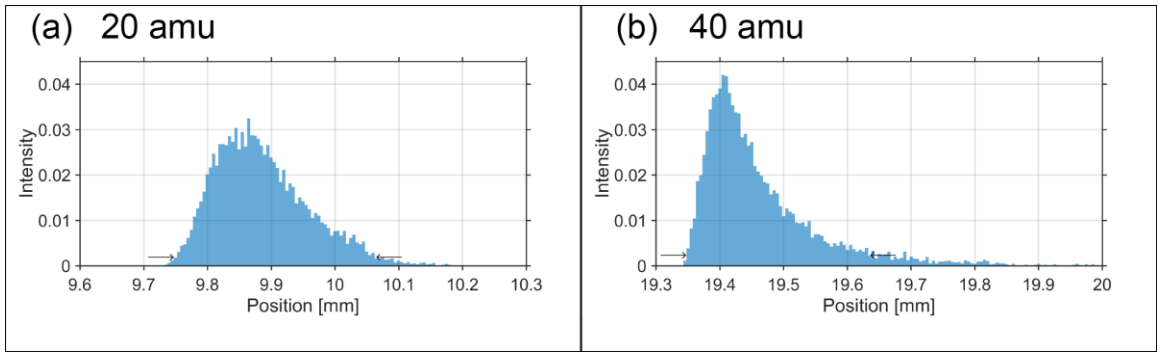

Figure 9: (a) Configuration 1 Resolving Power for 20 amu (b) Configuration 1 Resolving Power for 40 amu. The arrows on each figure indicate 5 % of maximum height.

The resolving power was estimated to be 0.32 mm for this sector configuration for 40 amu, and 0.37 mm for 20 amu, as seen in Figure 9a and Figure 9b. Note that for perfectly uniform magnetic and electric fields, the resolving power should be 0.05 mm, which is the width of the slit, and should be identical for any mass. In this case, however, since the electric field is not uniform especially around the ion source region, the resolving powers of particles at 20 amu and 40 amu are different.

These resolving powers were converted to the amu unit scale using Equation 1.1. For 20 amu particle trajectory, the resolving power was calculated to be 0.72 amu, while for 40 amu particle trajectory, the resolving power was calculated to be 0.63 amu.

3.2 2D analysis

In order to investigate various sector configurations expected to improve performance and determine how each of them affect the electric field profile, simulations were conducted in 2-dimensional space to expedite the process of finding a suitable configuration. The various configurations discussed in this subsection are a subset of all configurations attempted that yielded useful information regarding electric field uniformity.

3.2.1 Original Configuration

First, configuration 1 presented in the previous subsection was converted into a 2-dimensional sector to provide a basis for electric field profile analysis.

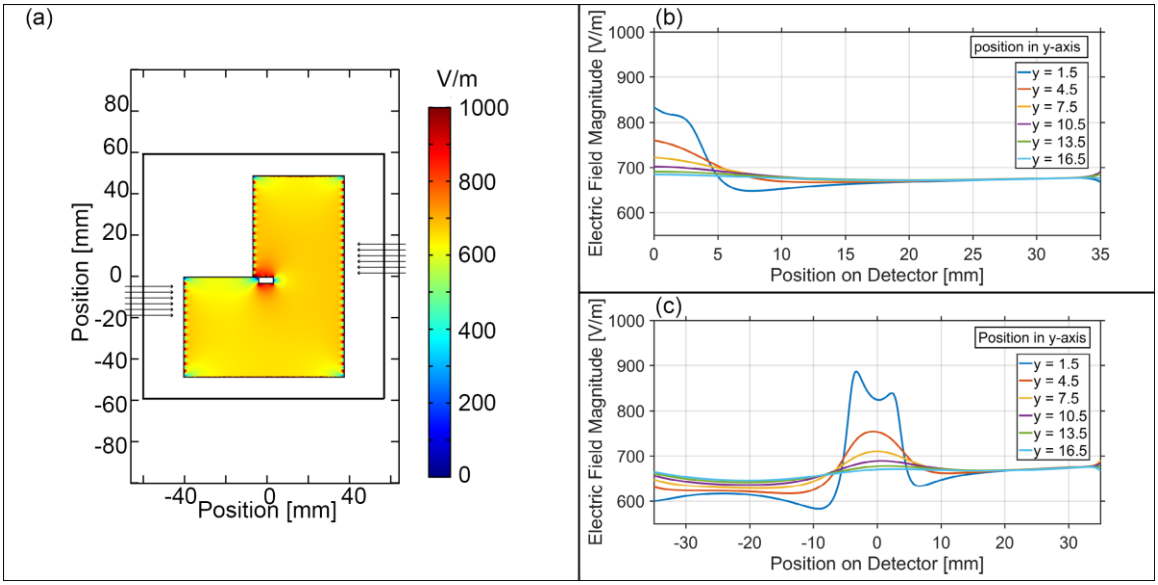

Figure 10: (a) 2-dimensional configuration 1 electric field magnitude (b) electric field magnitude around the upper region of the ion source, shown by the cutlines to the right axis in (a). (c) electric field magnitude around the lower region of the ion source, shown by the cutlines to the left axis in (a).

Similar to the results from the 3-dimensional analysis in the previous subsection, the electric field magnitude around the ion source region is not uniform as seen in Figure 10**b** and Figure 10**c**.

3.2.2 Modified Configuration A

The first attempt at improving the electric field around the ion source region involved shifting the position of the ion source. The hypothesis was that if the voltage on the ion source was similar to the potentials on nearby electrodes, the electric field uniformity would be better.

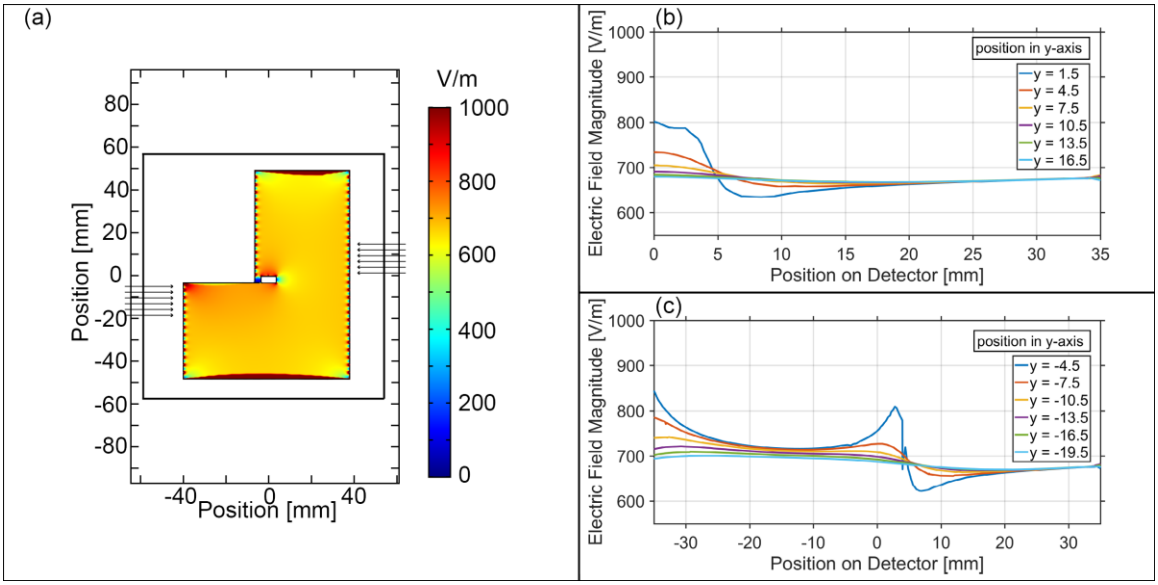

Figure 11: (a) 2-dimensional sector electric field magnitude profile (b) electric field magnitude around the upper region of the ion source, shown by the cutlines to the right axis in (a). (c) electric field magnitude around the lower region of the ion source, shown by the cutlines to the left axis in (a).

Figure 11 above shows the first configuration to test such hypothesis. Note that in Figure 11**a**, the ion source was moved 3 mm in the positive y axis (upwards) from the position demonstrated in Figure 10**a** of configuration 1. Note that the entire ion source is still grounded. Comparing Figure 10**b** and Figure 11**b**, the electric field magnitude above the ion source is essentially the same. However, comparing Figure 10**c** and Figure 11**c**, there is an improvement in uniformity of electric field magnitude for this new configuration. This observation can be explained by the fact that the ion source and the electrode nearest to the bottom of the ion source are both grounded. Since there is no potential difference between the ion source and the electrode closest to the bottom of the ion source, this region exhibits much smoother electric field uniformity.

3.2.3 Modified Configuration B

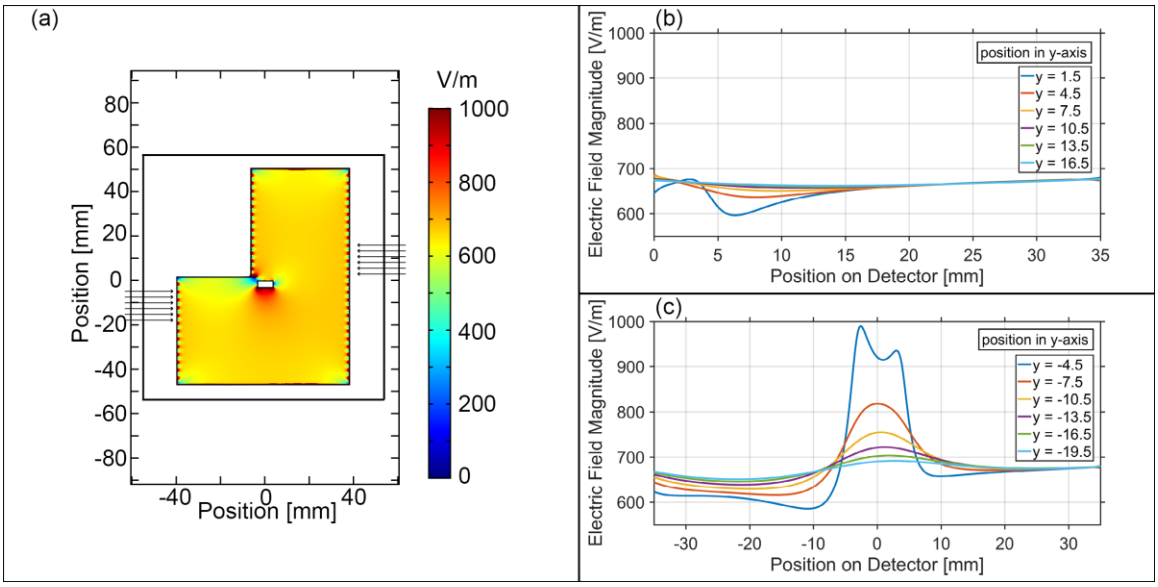

Figure 12: (a) 2-dimensional sector electric field magnitude profile (b) electric field magnitude around the upper region of the ion source, shown by the cutlines to the right axis in (a). (c) electric field magnitude around the lower region of the ion source, shown by the cutlines to the left axis in (a).

Figure 12**a** above illustrates another configuration of the sector to test the hypothesis that if the voltage on the ion source is similar to the potentials on nearby electrodes, the electric field uniformity would be better. This time, the ion source was moved 3 mm in the negative y-axis (downwards) compared to the location shown in Figure 10**a**. Note that the entire ion source is still grounded. Comparing Figure 10**c** and Figure 12**c**, the electric field uniformity is worse for this newer configuration. This is because in this newer configuration, the potential difference between the bottom of the

ion source and the nearest electrode is greater than that of configuration 1. Comparing Figure 10**b** and Figure 12**b**, note that the electric field uniformity in the region above the ion source is much better for this newer configuration. Once again, this observation can be explained by the fact that the potential difference between the top of the ion source and the nearest electrode is much smaller than that of configuration 1.

3.2.4 Modified Configuration C

With the knowledge that a smaller potential difference between the ion source and neighboring electrodes improves electric field uniformity, the next step was to determine a suitable location for the ion source such that both the top and bottom regions of the ion source would have significantly better field uniformity compared to configuration 1.

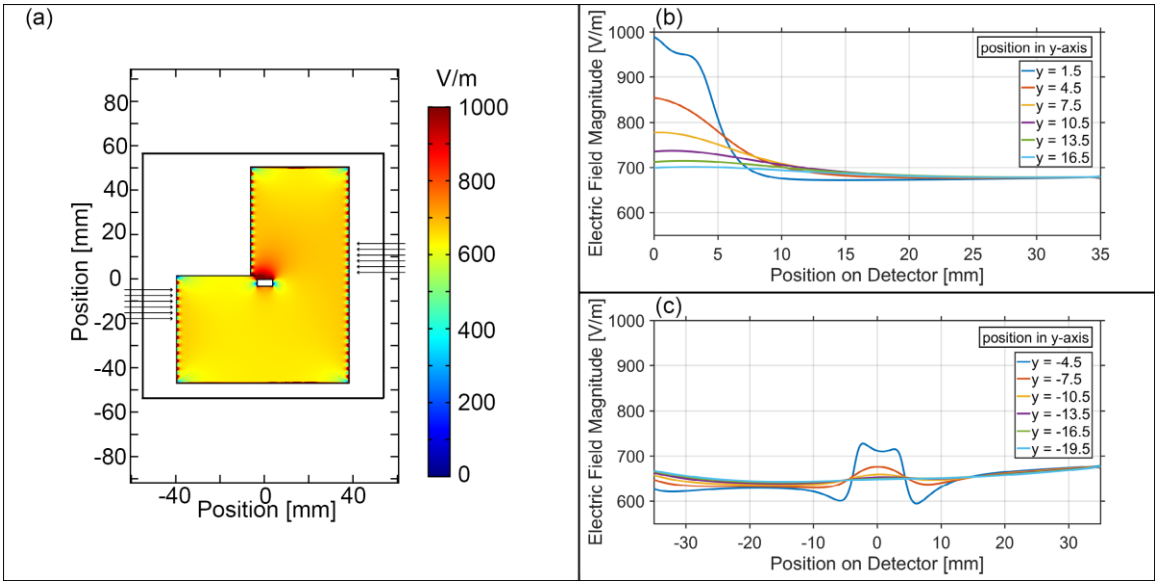

Figure 13: (a) 2-dimensional sector electric field magnitude profile (b) electric field magnitude around the upper region of the ion source, shown by the cutlines to the right axis in (a). (c) electric field magnitude around the lower region of the ion source, shown by the cutlines to the left axis in (a).

For all previous sector configurations, the ion source has been level with the nearest electrode. For this configuration, the ion source has been placed midway between two neighboring electrodes. The ion source is biased at the same potential as that of the electrode closest to the bottom of the ion source. Consistent with the observations from previous configurations, the lower area of the ion source has improved uniformity as seen in Figure 13**c** because the ion source has been biased at the same potential as the nearby electrode. Also, note that Figure 13**c** shows more uniformity than Figure 11**c**, even though for both configurations the ion source is biased at the same potential as the electrode closest to its bottom. It seems that placing the ion

source midway between two electrodes, rather than placing the source level with an electrode, has a more positive impact on electric field uniformity. Note that since the electrode closest to the top of the ion source is biased at a different potential, the field uniformity in that region is poor as seen in Figure 13**b**.

3.2.5 Modified Configuration D

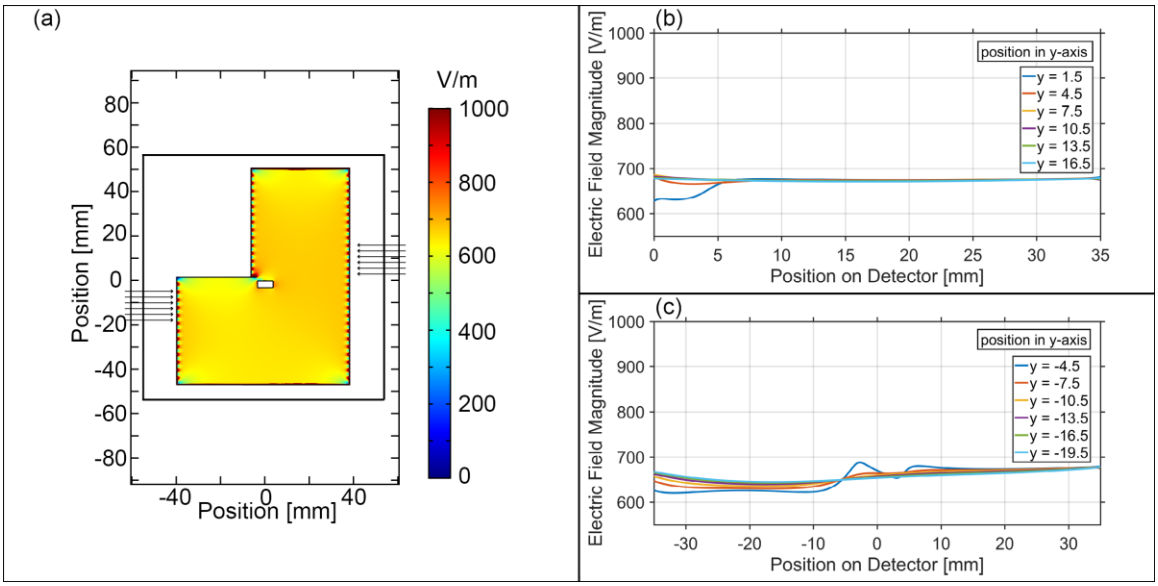

Figure 14: (a) 2-dimensional sector electric field magnitude profile (b) electric field magnitude around the upper region of the ion source, shown by the cutlines to the right axis in (a). (c) electric field magnitude around the lower region of the ion source, shown by the cutlines to the left axis in (a).

In order to have consistent electric field uniformity above and below the ion source, the top and bottom of the ion source were biased at different voltages to match those of nearby electrodes. In other words, the top of the ion source has been biased at

the same potential as that of the electrode closest to it, and the bottom of the ion source has been biased at the same potential as that of the electrode closest to it. This configuration yielded the most uniform field profile thus far, as seen in Figure 14**b** and Figure 14**c**. From previous configurations, we have determined that placing the ion source midway between electrodes and biasing the ion source at potentials close to those of the neighboring electrodes improve electric field uniformity. This configuration combines these two features by placing the ion source between two nearby electrodes and biasing the top and bottom of the ion source at potentials matching those of nearby electrodes. The result, as aforementioned, is that the field uniformity has been improved in both the top and bottom regions of the ion source. We decided that from here, we should continue simulations in 3-dimensional space again to ensure that the innovations from these previous configurations hold in 3-D as well. Thus, this configuration is referred to as "Configuration 2" in the remainder of the thesis.

3.3 Configuration 2

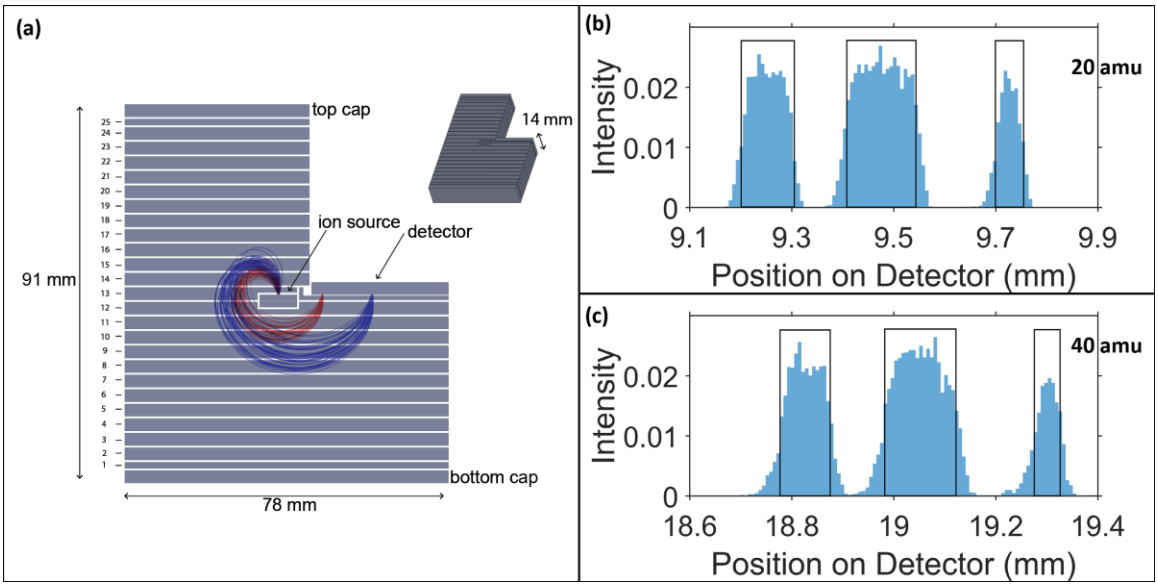

Figure 15: (a) Configuration 2 Electric Sector. Red lines represent 20 amu ion trajectory while blue lines represent 40 amu ion trajectory (b) Configuration 2 Imaging Quality at Detector for 20 amu (c) Configuration 2 Imaging Quality at Detector for 40 amu.

Figure 15**a** shows the novel electric sector configuration. The overall electric sector design is comparable to that of configuration 1. The sector is an L-shaped box of dimensions 91 x 78 x 14 mm. There are 28 electrodes, spaced 0.5 mm apart; 3 of these electrodes are 1.5 mm wide, while the rest are 3 mm wide. The main difference is that the ion source is now placed midway between neighboring electrodes. Moreover, the top and bottom of the ion source are biased at different voltages to match those of nearby electrodes. The rest of the electrodes were biased in the same manner discussed in the Methods section, using Equation 1.3.

This configuration yields aperture pattern images as seen in Figure 15**b** and Figure 15**c**. Note that compared to the images shown in Figure 1 for Configuration 1, a much smaller percentage of ions fall outside the S-11 aperture pattern denoted by the black rectangles and the imaging quality is significantly improved.

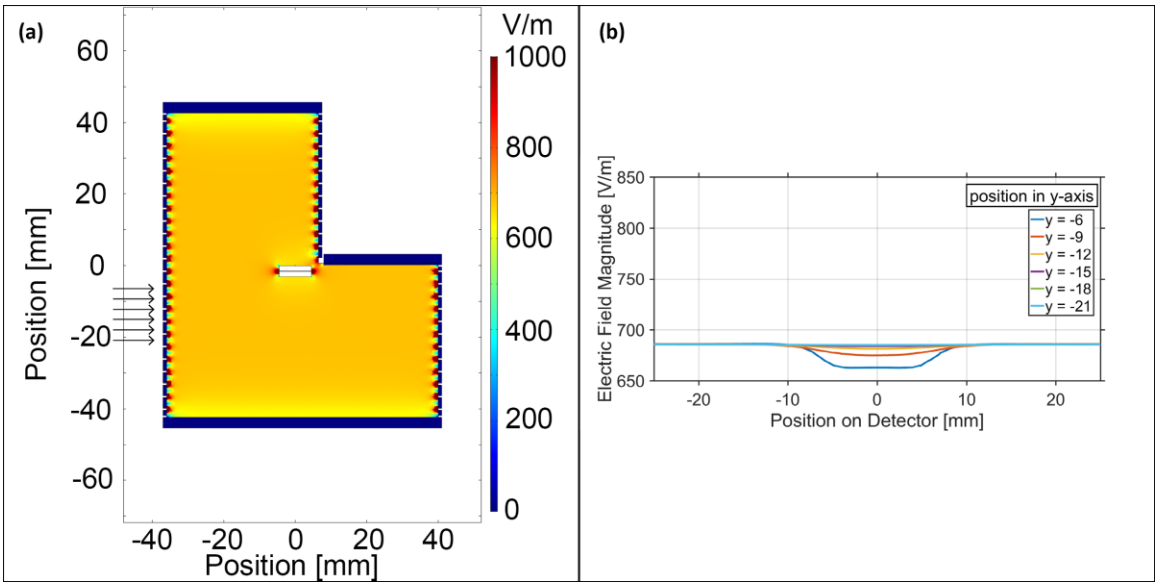

Figure 16: (a) Configuration 2 Electric Field Magnitude Profile (b) Configuration 2 Electric Field Magnitude Near Ion Source Region

Figure 16**a** shows the electric field magnitude of the configuration 2 electric sector. Since the top and bottom of the ion source are biased to match the potentials of nearby electrodes, the field uniformity is noticeably better around that region. Figure 16**b** shows the electric field magnitude around the ion source. Each line is a cutline across the sector, represented by the arrows in Figure 16**a**. Note that while the field

profile is not completely uniform, the variation is less than 5 %. Unlike the noticeable difference in imaging quality between 20 amu and 40 amu for configuration 1, in this case the difference is less conspicuous from Figure 16**b** and Figure 16**c**. This is because the electric field around the ion source is much more uniform, and thus the particles' cycloidal trajectory is not affected to the same degree.

Once again, in order to calculate the resolving power of this novel sector configuration, another set of simulations was run with a 0.05 by 1 mm slit.

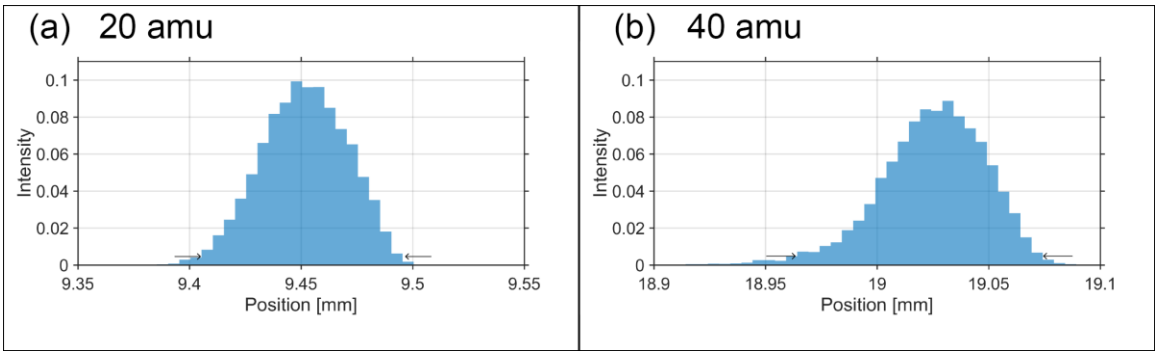

Figure 17: (a) Configuration 2 Resolving Power for 20 amu (b) Configuration 2 Resolving Power for 40 amu. The arrows on each figure indicate 5 % of maximum height.

Then, the slit image data at the detector plane was exported and the resolving power was calculated to be 0.10 mm for 40 amu and 0.07 mm for 20 amu as seen in Figure 17**a** and Figure 17**b**. Using perfectly uniform electric and magnetic fields, the resolving power would be equal to the slit width, which is 0.05 mm. Converting the units to amu using Equation 1.2, the resolving power is Note that the resolving power of configuration 2 is noticeably closer to this ideal value than configuration 1 (0.32 mm and 0.37 mm resolving power for 40 amu and 20 amu respectively).

Converting these resolving powers into the amu unit scale using Equation 1.1, the 20 amu particle trajectory had a resolving power of 0.14 amu while the 40 amu particle trajectory had a resolving power of 0.20 amu.

3.4 Voltage Variation

The resistors utilized in biasing each electrode of the sector will not be ideal. This is to say that under realistic conditions, the voltage on the electrodes may differ slightly from those utilized in simulations described in previous sections of this manuscript. More specifically, the resistors utilized in the laboratory prototype of the overall CAMMS-ES device are 20 kΩ with an uncertainty of 0.01 %. To test Configuration 2 under more practical settings, a 1 % variation in voltage was applied to each electrode. The resolving power of the sector was calculated for 20 amu and 40 amu particles.

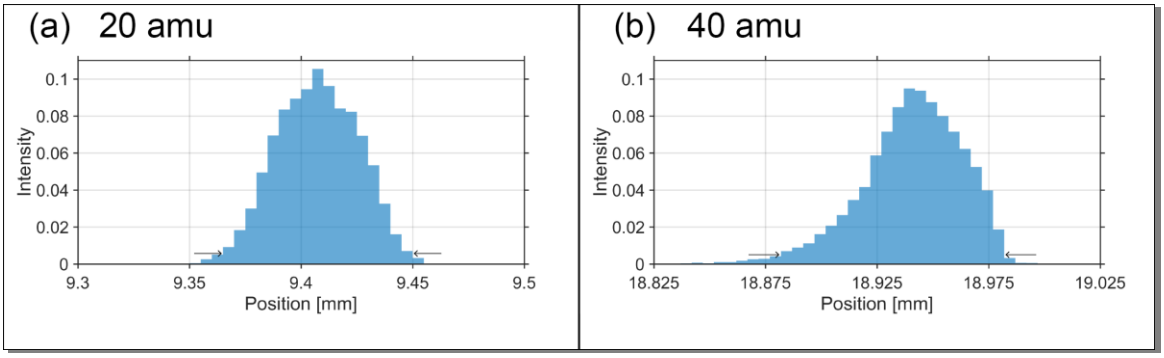

Figure 18: (a) Configuration 2 Resolving Power for 20 amu with voltage variation (b) Configuration 2 Resolving Power for 40 amu with voltage variation. The arrows on each figure indicate 5 % of maximum height.

For particle mass of 20 amu, the resolving power was calculated to be 0.08 mm, and for particle mass of 40 amu, the resolving power was calculated to be 0.10 mm. Note that these numbers are comparable to those calculated from ideal voltage conditions, which are 0.10 mm and 0.07 mm for 40 amu and 20 amu respectively.

Converting these resolving powers into the amu unit scale using Equation 1.1, the resolving powers were calculated to be 0.16 amu and 0.20 amu for 20 amu and 40 amu particle trajectories respectively.

4. Conclusion

In conclusion, a cycloidal mass analyzer's compatibility with aperture coding was increased by developing a novel electric sector configuration that improved electric field uniformity. By placing the ion source midway between neighboring electrodes, the electric field uniformity, especially around the ion source region, improved in configuration 2. Quantitatively, configuration 2 yielded better resolving power than configuration 1. More specifically, configuration 2 yielded an average resolving power of 0.085 mm, or 0.18 amu (for 20 amu and 40 amu), while configuration 1 yielded an average resolving power of 0.345 mm, or 0.675 amu.

References

1. Frish, M. METHAN LEAK DETECTION SYSTEM. (accessed 03/16).

2. McKenzie, L.M., Witter, Roxana Z., Newman, Lee S., Adgate, John L.: Human health risk assessment of air emissions from development of unconventional natural gas resources. Science of the Total Environment **424**, 79-87 (2012)

3. McCarthy, G., Method 325A-Volatile Organic Compounds from Fugitive and Area. Agency, E.P., Ed. 2015.

4. Chen, E.X., Russell, Z.E., Amsden, J.J., Wolter, S.D., Danell, R.M., Parker, C.B., Stoner, B.R., Gehm, M.E., Glass, J.T., Brady, D.J.: Order of Magnitude Signal Gain in Magnetic Sector Mass Spectrometry Via Aperture Coding. J. Am. Soc. Mass Spectr. **26**, 1633-1640 (2015)

5. Russell, Z.E., Chen, E.X., Amsden, J.J., Wolter, S.D., Danell, R.M., Parker, C.B., Stoner, B.R., Gehm, M.E., Brady, D.J., Glass, J.T.: Two-Dimensional Aperture Coding for Magnetic Sector Mass Spectrometry. J. Am. Soc. Mass Spectr. **26**, 248-256 (2015)

6. Russell, Z.E., DiDona, S.T., Amsden, J.J., Parker, C.B., Kibelka, G., Gehm, M.E., Glass, J.T.: Compatibility of Spatially Coded Apertures with a Miniature Mattauch-Herzog Mass Spectrograph. J. Am. Soc. Mass Spectr. **27**, 578-84 (2016)

7. Amsden, J.J., Herr, P.J., Landry, D.M.W., Kim, W., Parker, C.B., Kirley, M.P., Keil, A.D., Gilchrist, K.H., Radauscher, E.J., Hall, S.D., Carlson, J.B., Baldasaro, N., Stokes, D., Dona, S.T.D., Russell, Z.E., Grego, S., Edwards, S.J., Sperline, R.P., Denton, M.B., Stoner, B.R., Gehm, M.E., Glass†, J.T.: A first generation coded aperture miniature mass spectrometer for environmental sensing using a cycloidal mass analyzer, CNT field emission, and an array detector. In preparation

8. Bleakney, W., Hipple, J.A., Jr.: A New Mass Spectrometer with Improved Focusing Properties. Phys. Rev. **53**, 521-529 (1938)

9. Robinson, C.F.: Nonuniform Fields in Cycloidal-Focusing Mass Spectrometers. Rev. Sci. Inst. **27**, 509 (1956)

10. Landry, D.M.W., Amsden, J.J., Dona, S.T.D., Choi, H., Haley, L., Russell, Z.E., Parker, C.B., Glass, J.T., Gehm, M.E.: Novel permanent magnet assembly with improved field uniformity for cycloidal mass analyzers. In preparation

11. Blase, R.C., Miller, G., Westlake, J., Brockwell, T., Ostrom, N., Ostrom, P.H., Waite, J.H.: A compact E × B filter: A multi-collector cycloidal focusing mass spectrometer. Rev. Sci. Inst. **86**, 105105 (2015)

12. Herr, P.J., Radauscher, E.J., Parker, C.B., Gilchrist, K.H., Dona, S.T.D., Hall, S.D., Carlson, J.B., Grego, S., Edwards, S.J., Sperline, R.P., Denton, M.B., Stoner, B.R., Glass, J.T., Amsden, J.J.: A Miniature Carbon Nanotube Electron Ionization Source for Mass Spectrometry Applications. In preparation.

13. Todd, F.J.J.: Recommendations for Nomenclature and Symbolism for Mass Spectrometry. Pure and Applied Chemistry **63**, 1541-1566 (1991)